Int. J. Electrochem. Sci., 8 **(2013)** 7591 - 7607

International Journal of
ELECTROCHEMICAL
SCIENCE
www.electrochemsci.org

Improve on Corrosion Resistant Surface for AISI 4140 Steel Coated with VN and HfN Single Layer Films

C. Escobar[1], *J. C. Caicedo*[1,2,*], *W. Aperador*[3], *A. Delgado*[3,4], *P. Prieto*[1, 5]

[1]Departamento de física, Universidad del Valle, Ciudad Universitaria Meléndez, Calle 13 #100-00 Edificio 320, A.A. 25360 Cali, Colombia
[2]Tribology Polymers, Powder Metallurgy and Processing of Solid Recycled Research Group Universidad del Valle, Cali – Colombia
[3] Facultad de Ingeniería, Universidad Militar Nueva Granada, Bogotá – Colombia
[4]Facultad de Ingeniería Industrial, Escuela Colombiana de Ingeniería, Bogotá – Colombia.
[5]Centro de Excelencia en Nuevos Materiales, Calle 13 #100-00 Edificio 320, espacio 1026, Cali, Colombia
[*]E-mail: g.ing,materiales@gmail.com

Received: 10 April 2013 / *Accepted:* 13 May 2013 / *Published:* 1 June 2013

To improve the corrosion resistance of different industrials application, we studied vanadium nitride (VN) and hafnium nitride (HfN) single layer thin film, which were deposited onto Si (100) and AISI 4140 steel substrates via r.f. magnetron sputtering technique in Ar/N_2 atmosphere with purity at 99.99% for both V and Hf metallic targets. Both films were approximately 1.2 ± 0.1 µm thick. The crystallography structures that were evaluated via X-ray diffraction analysis (XRD) showed preferential orientations in the Bragg planes VN (200) and HfN (111). The chemical compositions for both films were characterized by EDX. Atomic Force Microscopy (AFM) was used to study the morphology; the results reveal grain sizes of 78 ± 2 nm for VN and 58 ± 2 nm for HfN and roughness values of 4.2 ± 0.1 nm for VN and 1.5 ± 0.1 nm for HfN films. The electrochemical performance in VN and HfN films deposited onto steel 4140 were studied by Tafel polarization curves and impedance spectroscopy methods (EIS) under contact with sodium chloride at 3.5 wt.% solution, therefore, it was found that the corrosion rate decreased about 95% in VN and 99% for HfN films in relation to uncoated 4140 steel, thus demonstrating, the protecting effect of VN and HfN films under a corrosive environment.

Keywords: Sputtering; X-ray diffraction, Atomic Force Microscopy, Electrochemical properties.

1. INTRODUCTION

Cutting tools are exposed to elements such as water, oxygen, and ions in an industrial environment. The protection of these tools from corrosion has become a very important issue from an

economical viewpoint. Surface modification by applying a thin film is an important industrial process used to protect base materials against corrosion and many other surface related damages. The modern methods of physical vapor deposition techniques (PVD) provide great flexibility for designing films with a specific chemistry and microstructure, leading to coatings with unique properties [1,2]. Transition metal nitride coatings are widely used in the wear and corrosion resistant layer of the tool components. Previous studies report the concept of layers offers a potent solution for physical, tribological and chemical properties in hard coatings. The coatings deposited via PVD based on nitrides (TiCN [1], AlCN [3], CrAlN [4], TiWN [5], and oxides such as YSZ [2], $BiMnO_3$ [6]) provide high wear resistance, stability under high service temperature, oxidation and corrosion resistance. Vanadium nitrides (VN) are commonly used components in multifunctional coatings combining hardness [7], wear and low-friction properties [8,9], and corrosion resistance [10]. In all these applications the coating performance is strongly affected by surface roughness and film texture, which not only influence the tribo-mechanical properties but also the chemical behavior. Oxidation is a key factor during the handling of coated surfaces since the degradation of coatings occurs by a mixture of wear, diffusion and surface oxidation processes [11]. Hafnium nitride (HfN) (like all nitrides of the transition metals) is a promising alternative material in many regards because of its excellent properties such as superior mechanical property [12], high melting temperature (3387 ºC), good electrical conductivity and acceptable oxidation resistance in extreme environments (it begins to oxidize in air at approximately 800ºC) [13], which was widely used as a diffusion barrier [14], hard coating and wear-resistant coating [15]. Current literature reports few results of the corrosion performance of VN and HfN thin films exposed to an aggressive environment. Therefore, the purpose of this work is to study the electrochemical nature (corrosion resistance) of these materials deposited on AISI 4140 steel substrates by using electrochemical impedance spectroscopy (EIS) and polarization methods (Tafel). In this sense, the present research shows the HfN and VN single layer thin films are a potential alternative in the surface protection of AISI 4140 steel material.

2. EXPERIMENTAL

VN and HfN single layer thin films were grown onto Si (100) and AISI 4140 steel substrates using a multi-target magnetron sputtering system. The AISI 4140 steel discs with a diameter of 12.5 mm used as substrates were cut with a total thickness of 5 mm and were mechanically polished by using 1 μm grit Al_2O_3. The chemical composition of the steel used in this work is listed in Table 1. The samples were cleaned via ultrasonic washing in acetone for 5 minutes. VN and HfN thin films were deposited by reactive magnetron sputtering with an r.f. source (13.56 MHz). The plasma cleaning procedure was used for all substrates under argon atmosphere. Two Hf and V metallic targets with 99.9% purity were used as source materials. The deposition parameters to obtain HfN and VN films had a sputtering power of 400 W for V and 350 W for the Hf target; an unbalanced r.f. bias voltage was applied, which generates a negative signal fixed at -30 V, and a substrate temperature of 250 ºC under 60 rpm circular rotation substrate to facilitate the formation of the stoichiometric films. The sputtering gas was a mixture of Ar 80% and N_2 20% with a total working pressure of 0.12 Pa. Film

thickness was measured about 1.2 ± 0.1 μm, determined by means of a (Dektak 3030) Profilometer. The crystal structure of the films was determined by using a Panalytical X'Pert PRO X-ray diffractometer with Cu-Kα radiation (λ = 1.5405 Å). The crystallographic structure simulation was designed with CaRIne v3.1 software for the VN and HfN thin films. Chemical composition analysis of the films was conducted using a JSM 6490 LV JEOL scanning electron microscopy, an X-ray detector and a secondary electrons detector of Lithium Beryllium inside the chamber with the purpose of amplifying the signal in the energy-dispersive X-ray spectroscopy (EDX) analysis. Due to EDX having a low reliability for nitrogen concentration, a careful correction must be done in all stoichiometric analysis. Therefore, EDX elemental concentrations were obtained by using the ZAF correction method; because certain factors related to the sample composition, namely matrix effects associated with atomic number (Z), absorption (A) and fluorescence (F), can affect the X-ray spectrum produced during the analysis of electron microprobe. Therefore, these effects should be corrected to ensure an appropriate analysis. The correction factors for a standard specimen of known composition were determined initially by the ZAF routine. The relative intensity of the peak K was determined by dead time corrections and a referent correction for the X-ray measured. Thus, before each quantitative analysis of an EDX spectrum, a manual background correction and an automated ZAF correction was completed [16]. SEM-EDX technique was used for determination of chemical composition in steel substrate (Table1) and (VN and HfN films). Microstructural analysis of films was mainly performed by TEM, using a Philips CM30 microscope operating at 300 kV. Morphologic characteristics of the single film like grain size and roughness were obtained by using an Atomic Force Microscopy (AFM) from Asylum Research MFP-3D® and calculated by a Scanning Probe Image Processor (SPIP®) [17]. The electrochemical study was carried out using a Garmy unit; model PCI 4, utilized for DC and AC measurements. Electrochemical Impedance Spectroscopy (EIS) and Tafel polarization curves were obtained at room temperature (25 C) in static conditions (without aeration), using a cell with a working electrode of an exposed area of 1 cm^2, Ag/AgCl (3.33 M KCl) reference electrode and a platinum wire counter-electrode under a 3.5 wt.% NaCl solution with distilled water at pH 6.2. For Bode plot, frequency sweeps were conducted in the range of 100 kHz to 0.001 Hz using sinusoidal signal amplitude of 10 mV applied to the working electrode (sample) and reference electrode. Diagrams for Tafel polarization curves were obtained at a sweep speed of 0.125 mV/s in a voltage range from -0.25 to 0.25 $V_{Ag/AgCl}$, this voltage range was defined with respect to the open circuit potential (OCP). Prior to beginning the polarization curves procedures, the samples were submerged in the 3.5 wt.% NaCl aqueous solution for 30 minutes in order to establish the free corrosion potential values (E_{corr}) at which the polarization curves measurements were initiated. Finally, to identify the corrosion process scanning electron microscopy images and EDX analysis were used.

Table 1. Chemical composition of AISI 4140 steel in weight percent (wt.%), (Fe, Mn, C and Cr peaks).

C	Mn	P	S	Si	Cr
0.41	0.81	0.21	0.040	0.10	0.13

3. RESULTS AND DISCUSSION

3.1. X-ray diffraction analysis

Both single layers have a similar thickness of 1.2± 0.1 µm. Taking into account the previous result, the crystallographic structures of VN and HfN films were obtained by X-ray diffraction. Fig. 1a shows the XRD pattern of VN films deposited with an r.f. negative bias voltage of -30 V on Si (100) substrate. The XRD pattern shows a high intense Bragg peak at $2\theta = 43.91°$ corresponding to reflections in the (200) planes which indicate a high grade of crystallinity along this orientation; other Bragg peaks with lower intensity at $2\theta = 37.83°$ and $2\theta = 63.91°$ were associated with reflections in the (111) and (220) planes, respectively [18]. Therefore, the aforementioned orientations correspond to a structure face-centered cubic (FCC) NaCl-type Fm3m related to the δ-VN phase. The latter is in agreement with JCPDS 00-035-0768 from ICDD card. Fig. 1b shows the XRD pattern of HfN film deposited with an r.f. negative bias voltage of -30 V on Si (100); the XRD pattern presents a cubic structure where the strongest peak at $2\theta = 34.40°$ corresponds to the HfN (111) plane, indicating a light textured growth along this orientation. The other weak peaks correspond to diffractions from (200) and (220) planes of the face-centered cubic (FCC) NaCl-type Fm3m structure that were identified at $2\theta = 39.74°$ and $2\theta = 57.39°$, respectively. Those orientations were related to the δ-HfN phase in agreement with JCPDS 00-033-0592 from HfN (δ-HfN) ICDD cards. Also noted was a Bragg peak at $2\theta = 34.26°$ associated with the Hf buffer layer at (100) planes according to JCPDS 00-038-1478 from ICDD card.

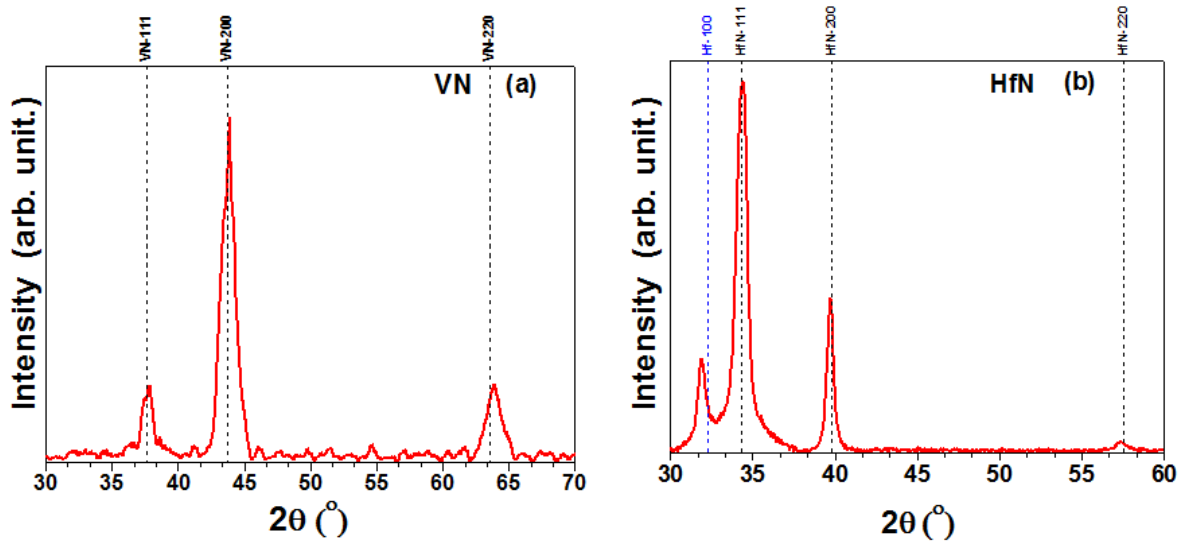

Figure 1. Diffraction patterns: (a) VN, (b) HfN films grown on Si (100). Dash lines indicate the position of the peaks in agreement with JCPDS files obtained from ICDD cards.

3.2. EDX analysis

The Energy-dispersive X-ray spectroscopy (EDX) was used to determine the chemical composition present in VN and HfN films deposited on the steel substrate. Both films were

homogenous in composition. An atomic concentration around 43% and 57% was found for the V and N, respectively. While for the Hf-N film was found an atomic concentration for the Hf and N around 44% and 56%, respectively, Table 2. In this work, EDX analysis shows that both films have overstoichiometric compositions ($V_{0.43}N_{0.57}$ and $Hf_{0.44}N_{0.56}$).

Table 2. Chemical composition of the V-N and Hf-N single layer films deposited on Si (100) substrates.

Films	V	Hf	N
VN	43	-	57
HfN	-	44	56

3.3. Crystalline structure and crystallographic orientation simulation for VN and HfN thin films.

From XRD it was possible to determine the lattice parameter for VN and HfN films. A value of $a_0 = 4.120$ Å (± 0.001 Å) and $a_0 = 4.511$ Å (± 0.001 Å) for VN and HfN films was obtained for the lattice parameter, respectively, where the Nelson–Riley function was employed in the refinement procedure. In the VN case the results show a compression of the cell unit respective to the value reported in the literature for VN in powder (4.132 Å) [19]. The value of the lattice parameter for the HfN films indicate a compression of the cell unit respective to the value reported in the literature for HfN in powder (4.525 Å) [13]. The latter behavior in the lattice parameter for both films was attributed to ions impact from Ar^+ which produces a compressive stress in both VN and HfN single layer films.

With the aim of verifying the crystalline structure and crystallographic orientation for VN and HfN single layer, a simulation by using CaRIne crystallography software version 3.1 was implemented. The software required input parameters such as occupation factor of the element that constitutes the film which are experimentally obtained from chemical composition determined via EDX analysis. Other parameters required for the simulation were the crystalline structure, space group, and lattice parameter (a_0) obtained from experimental XRD analysis for VN and HfN thin films which are in agreement with JCPDS files obtained from ICDD cards for those materials. Moreover, the ionic radius values for each element e.g. (V, Hf and N) were obtained from literature data [13]. In this sense, Table 3 shows input parameters used for simulation.

Results of theoretical structural tests reveal simulated XRD patterns (Fig. 2a and Fig. 2c) which show similar crystalline characteristics, but with different preferential orientations, exhibiting the (200) Bragg plane as the preferential orientation for the VN film while the HfN films present a preferential orientation in (111) Bragg plane. Fig. 2b and Fig. 2d present a 3D-View of a crystallographic structure model obtained by using CaRIne v3.1 software. The 3D-View of the crystallographic representation (Fig. 2b and 2d) is associated with VN and HfN thin films, respectively; where, FCC crystalline structures are shown, which have V and Hf atoms in the (0 0 0) positions while the N atoms are placed in the (1/2 1/2 1/2) octahedral positions in agreement with the XRD results.

Table 3. Experimental and theoretical values used in the crystallographic simulation.

Material	Data source	Occupation percentages	Ionic radius (Å)	Crystalline Structure	Space Group	Lattice parameter (a_0) (Å)
HfN	EDX	$Hf_{0.44}$-$N_{0.56}$	-	-	-	-
	XRD and JCPDS00-033-0592	-	$Hf_{1.56}$-$N_{0.75}$	FCC	Fm3m	4.511
VN	EDX	$V_{0.43}$-$N_{0.57}$	-	-	-	-
	XRD and JCPDS00-035-0768	-	$V_{1.31}$-$N_{0.75}$	FCC	Fm3m	4.120

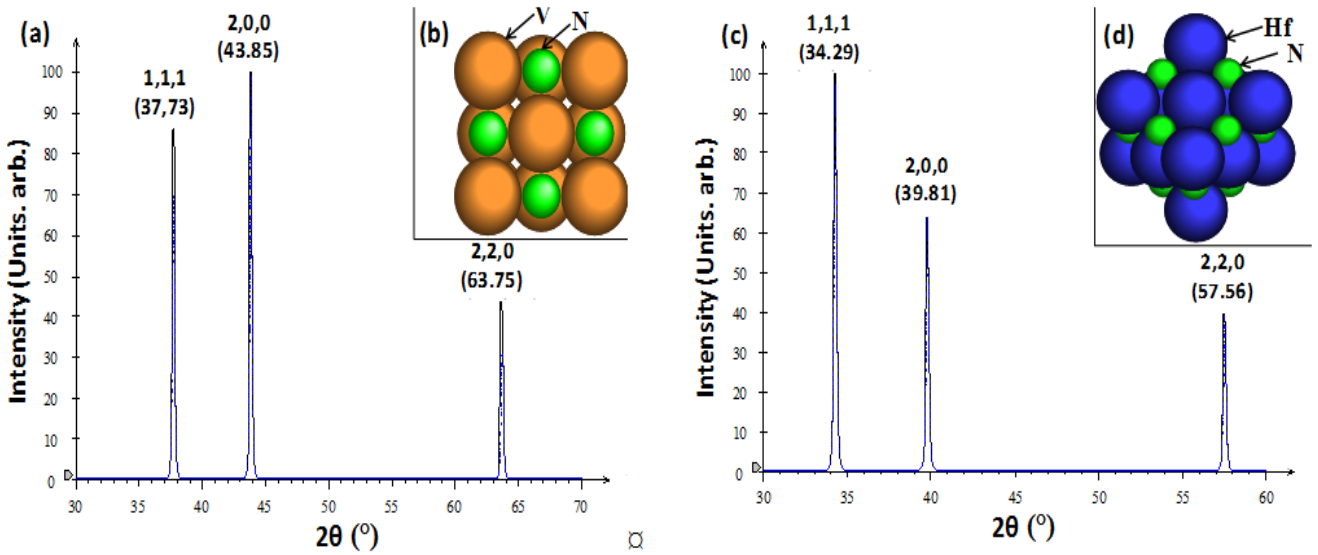

Figure 2. XRD pattern and crystalline structure simulated from CaRIne software for VN (a-b) and HfN (c-d) thin films.

Figure 3 compares the experimental XRD pattern obtained from Panalytical X'Pert PRO X-ray diffractometer with the simulated XRD pattern from CaRIne v3.1 software for VN and HfN films (Fig. 3a and Fig. 3b, respectively). This theoretical and experimental comparison allowed the match between the simulated and experimental patterns for all films. In Fig. 3 the dash lines represent the characteristic orientations shown for samples in powder in agreement with JCPDS 00-035-0768 to VN and JCPDS 00-033-0592 to HfN, taken from their ICDD cards, respectively. Moreover, in Fig. 3 it is possible to observe the preferential orientation in both films, a low shift toward high 2θ values in relation to JCPDS patterns, therefore, this effect can be attributed to a lattice mismatch due to compressive stress presented in the VN and HfN films, as a consequence of the deposition parameters specifically, by negative bias voltage applied to the substrate during film deposition.

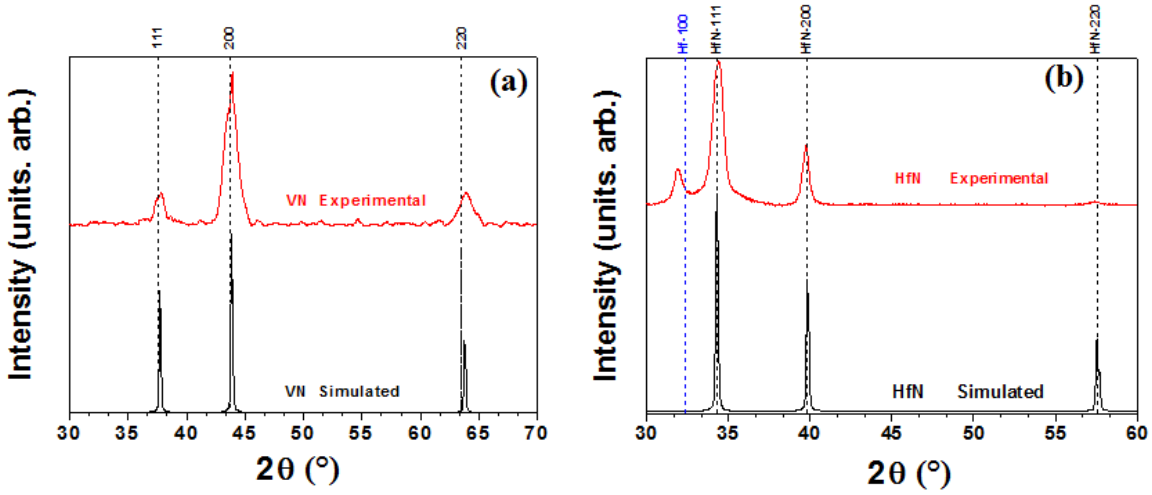

Figure 3. Comparison between simulated and experimental XRD patterns for the (a) VN and (b) HfN thin films.

3.4. Transmission electron microscopy analysis

A first glimpse of atomic coherence and microstructures was accomplished by HRTEM images. Fig. 4 presents the TEM cross-sectional image of an HfN and VN single films with 4 nm. The interplanar distance in both single layers was confirmed using transmission electron microscopy. All the single films stacks were resolved by TEM and confirmed quite precisely by the previously designed nominal crystallographic orientations. TEM images show in terms of the interplanar distance that HfN layer (d = 0.2612 nm) is higher than VN layer (d = 0.2063 nm); they also confirmed that for the interplanar distance in HfN and VN layer there is a different deviation of 0,0549 nm.

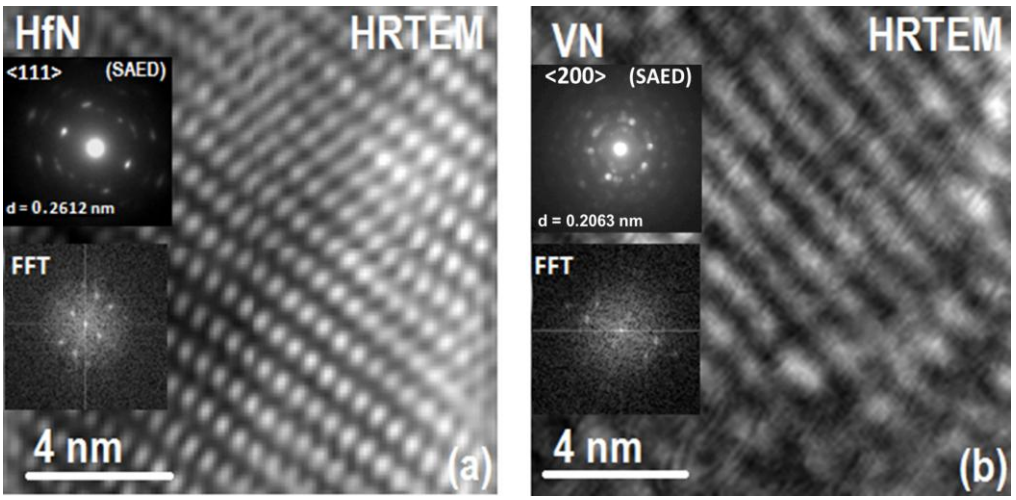

Figure 4. Atomic coherence and microstructures of HfN and VN layers by TEM image with SAED pattern and FFT simulations.

It reveals a compact crystalline structure with wide columnar grains extended along the entire single layers stack. The SAED pattern of the whole multilayer indicated a (111)-preferred orientation for HfN layer and a (200)-preferred orientation for VN layer, confirming the XRD results and XRD simulations. Also, the region shown in Fig. 4 enabled us to study the structure of a single crystallite, which can be identified as a small dark zone propagating through the film. The SAED patterns of a region overlapping several planes for both (VN and HfN) structures shows an array of regularly distributed spots respectively (Fig. 4), confirming together with XRD results and FFT simulations the expectations of a coherent single layer structures.

3.5. Morphological analysis by AFM

Atomic Force Microscopy (AFM) was employed to quantitatively study the surface morphology in the VN and HfN single layers deposited on Si (100) substrate. In this sense, a 1 μm x 1 μm area was analyzed for all films with a Z-scale around 26.03 ± 2.0 nm. Fig. 5a and Fig. 5b show the images taken in a non-contact mode for the VN and HfN films respectively. From these AFM images, the grain size and roughness values were extracted by using a Scanning Probe Image Processor (SPIP®). Therefore, it was possible to obtain the grain size values for VN (78 ± 2.0 nm) and HfN (58 ± 2.0 nm) single layers, roughness values around 4.2 ± 0.1 nm and 1.5 ± 0.1 nm to VN and HfN films, respectively. The differences in the roughness values can be attributed to differences in the interplanar distance observed in TEM results (Fig. 4.). From AFM results it is possible to observe that the surface for both single layers show lower roughness values than other nitrides deposited by the PVD technique [4,5]. The last effect, it was attributed to the (Ar^+) ion bombardment of the films which stimulated not only a greater number of nucleation places that produce a grain size reduction, but increased the film's density which produce an entire surface roughness diminution [5]. The latter is important because a smooth surface with good homogeneity in composition can help decrease the corrosion susceptibility when these layers are exposed in an aggressive environment [4].

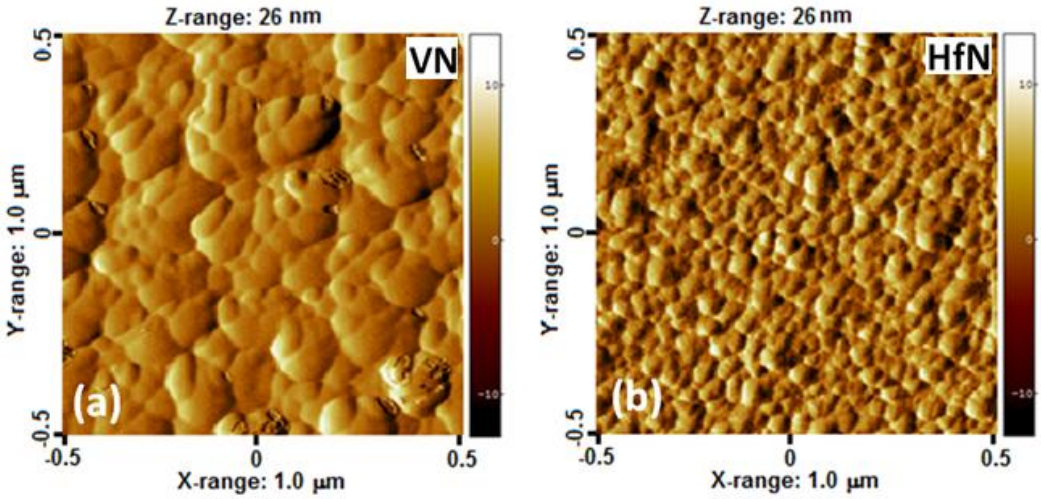

Figure 5. AFM images for nitride films deposited with an r.f. negative bias voltage of 30 V on Si (100) substrate. VN (a) and HfN (b) single layers.

3.6. Electrochemical impedance spectroscopy (EIS) and Tafel polarization curves of VN and HfN thin films

For the corrosion rate analysis, the corrosion rate was calculated after the previous determination of the current corrosion density, i_{corr}, by using the Stern–Geary equation [20]:

$$i_{Corr} = \frac{\beta_a \cdot \beta_c}{2.303 R_p (\beta_a + \beta_c)} \quad (1)$$

This approach suggests that the corrosion process studied takes place in the region of the active dissolution of the metal, due to that β_a and β_c are the Tafel slopes for the anodic and cathodic partial reactions, respectively, R_p is the polarization resistance value extracted from the impedance analysis. The total impedance of the system (Z) is given by the equation:

$$Z(\omega) = R_S + \frac{R_P}{1 + R_P \sigma (j\omega)^a} \quad (2)$$

Where R_s is the Ohmic resistance between the reference and working electrodes, ω is the applied angular frequency, σ is the proportionality parameter of the constant phase element (CPE), and $j = (-1)^{1/2}$. CPE is used for the simulation of the double-layer impedance. The double-layer impedance of a solid electrode represented by CPE is defined as:

$$Z_{CPE} = \sigma^{-1} (j\omega)^{-\alpha} \quad (3)$$

where σ^{-1} is a real adjustable constant used in the non-linear least squares (NLLS) fitting, and $-1 < \alpha < 1$ is defined as a CPE exponent [21]. When $\alpha = 0$, CPE is a resistor; when $\alpha = 1$, it is an ideal capacitor; and when $\alpha = -1$, it is an inductor. Finally, if $\alpha = 0.5$, CPE is the Warburg admittance. At $0 < \alpha < 1$, a depressed semicircle with a center below Z' axis should be observed. In the frame of this simplest model, R_p is expressed as:

$$R_P = \left|Z(j\omega)\right|_{\omega \to 0} - \left|Z(j\omega)\right|_{\omega \to \infty} \quad (4)$$

The depressed semicircle is generally due to a dispersion in the time constant caused by irregularities on the steel surface, surface roughness, fractal surface, and in general certain processes associated with an irregular distribution of the applied potential (10 $mV_{Ag/AgCl}$) to obtain EIS data.

Figure 6 shows the Bode plot, corresponding to the HfN film (blue filled triangle) and VN (red filled squared) single layers grown on AISI 4140 steel substrate with a negative bias voltage of -30V, and the uncoated AISI 4140 steel substrate (full circles). A complex non-linear least squares (NLLS) analysis was performed to fit the parameters of the equivalent circuit of Fig. 6 to the impedance data. The fitted parameters are listed in Table 4. As observed in Fig. 6, there is excellent agreement between the experimental and simulated results. From the Table 4 the polarization resistance values, R_p, in according with equation (4) for each sample were used to simulate the interface coating phenomenon, together with a double layer cell equivalent circuit (Fig. 7) [22,23]. So, in the double layer cell circuit, the substrate-coating and coating-electrolyte interfaces act as a double layer capacitance in parallel to the coating resistance and the electrolyte resistance, due to the Cl^- ion reaction transfer [22] from the electrolyte to the metallic substrate. Results in Table 4, indicate that polarization resistance increases for both VN and HfN films in relation to uncoated AISI 4140 steel. In this sense it is possible to observe that the polarization resistance for the HfN single layer is greater than that VN film. This effect is related to lower interplanar distance of the HfN film in comparison with VN film observed

from TEM results (Fig. 4), therefore, is possible to say that low interplanar distance value produces an approach of atomic planes producing a lower electrochemical potential of the (HfN) molecule, which prevents the progression of Cl^- ions generating thus an increased superficial protection.

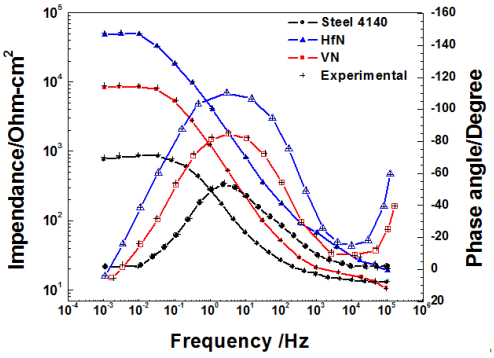

Figure 6. Bode plot of HfN and VN thin films grown on AISI 4140 steel with bias voltages of -30V.

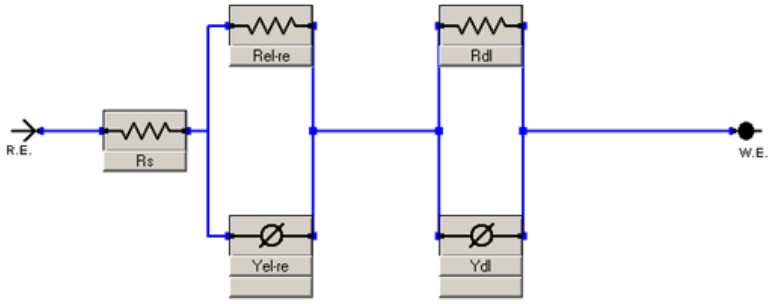

Figure 7. Equivalent circuits used for simulation of the experimental data in electrochemical characterization of HfN and VN single layer films. Solution resistance (Rs); resistance between electrolyte and coating (Rel-re); constant phase elements (Yel-re = CPE_1), (Ydl = CPE_2); films-substrate resistance (Rdl).

Table 4. Parameters obtained from the fitting of impedance data for the HfN and VN thin films grown on AISI 4140 steel substrate with bias voltages of -30V (Error is in brackets).

	R_s □ cm^2	Y_{p1} □F cm^{-2}	□□	R_1 10^3□ cm^2	Y_{p2} □F cm^{-2} $s^{-(1-□□□}$	□□	R_2 10^3□ cm^2
HfN	18.12 (0.5%)	8.06 (2%)	0.86 (0.2%)	9.25 (5%)	48.01 (2%)	0.73 (0.6%)	39.46 (6%)
VN	33.5 (0.3%)	6.54 (1.8%)	0.79 (0.3%)	1.09 (5%)	15.58 (4%)	0.87 (0.4%)	6.91 (5%)
Steel 4140	22 (0.8%)	2.88 (2.5%)	0.76 (0.9%)	8.07 (5%)	--	--	--

The electrochemical mechanism used by the electrolyte (NaCl) in the path to steel surface, was carried out by means of nano-pores. However, the HfN and VN films do not exhibit macroporosity before the corrosion test, as was observed previously by AFM analysis.

In this sense, the calculation of the porosity was developed at the atomic level and not at the macro level; otherwise, it would radically change the entire study, since the circuit would be different. Then, all fits were made to the Bode plots, so that these values correspond to the values given to the equivalent circuit used. Therefore, the fit is acceptable, as shown in the error of the measure, and in this view, the circuit used in this type of study is appropriate.

On the other hand, Figure 8 shows Tafel polarization curves (corrosion potential as a function of the corrosion current density) for the HfN and VN films. The corrosion resistance for HfN and VN materials in the polarization curve is determined by low current densities when the electric potential is increased. In this sense, the Tafel analysis is used quantitatively to determine the corrosion potential (E_{corr}), and the corrosion current density (i_{corr}) (equation 1). The last parameter is used to calculate the corrosion rate, CR, which can be expressed as:

$$CR = \frac{i_{corr} K \cdot E_W}{Ad} \qquad (5)$$

where K is a proportionality constant and E_w is the equivalent weight of the work electrode [20,24]. The general results of corrosion rate in the films are shown in Table 5. It observed a higher corrosion resistance of HfN and VN thin films because of more positives corrosion potentials and lower corrosion currents density in relationship to the uncoated AISI 4140 steel, confirming the protective effects of the single layer films. This behavior is related to low grain size, which was observed from AFM images in Fig. 5. Therefore, the low grain size generates an increase of the ion diffusion resistivity, because the zig-zag grain boundaries of fine structure (e.g. VN and HfN shown in Fig. 5) could result in a dramatic decrease in Cl^- ion across the electrolyte/coating interface.[25], and hence improve the corrosion resistance, reflecting a lower corrosion rate.

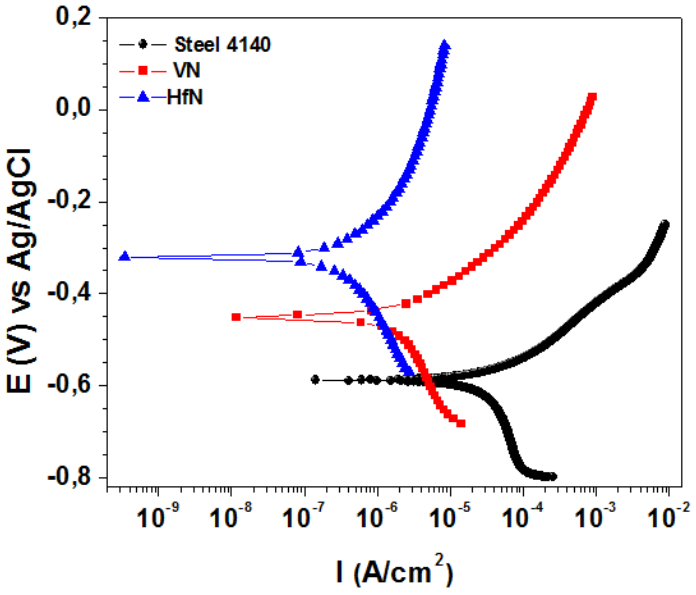

Figure 8. Tafel curves of HfN and VN single layer films grown on AISI 4140 steel.

Table 5. Parameters used to calculate the corrosion rate of HfN and VN single layer films grown on AISI 4140 steel with bias voltages of -30V.

	Ba 10^{-3} (V/dec)	*Bc* 10^{-3} (V/dec)	R_p (k□ cm^2)	i_{corr} ($\mu A/cm^2$)	v_{corr}(μmy)	Chi Squared 10^{-3}
Steel 4140	167.05	280.21	0.80	199.01	790.39	3.27
VN	34.80	52.70	8.49	0.53	40.87	2.66
HfN	180.41	260.70	49.34	0.19	0.205	9.95

In the Tafel polarization curves it is observed that the corrosion is uniform, but the mechanism used by the electrolyte (ions Cl^-) when they pass through the (HfN and VN) films and reach to the substrate is due to the nanoporosity presented by these systems. Moreover, all nitride films have porosity in relation to packing factor. In this sense an approximation of corrosive attack mechanism is present in the Fig. 9, which shows the path followed by Cl^- ions traveling from the coating to the substrate, causing delamination of the film.

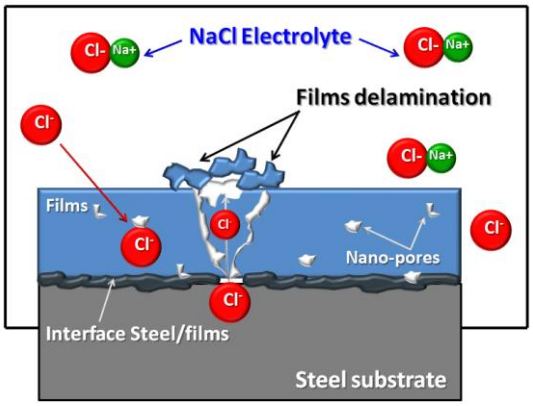

Figure 9. Corrosive mechanism generated by Cl^- ions on HfN and VN films deposited on steel AISI 4140 substrates.

3.7. SEM and EDX examinations

After the Tafel corrosion test, SEM images and EDX analysis (Fig. 10 and Fig. 11), respectively, were used to observe the different zones exposed in the corrode samples. Fig. 10a shows a SEM micrograph for steel substrate coated with HfN films under a corrosion processes with a NaCl solution. From SEM micrographs it was possible to identify three zones corresponding to the corrosive processes. In this sense, the EDX spectra was extracted from zone 1 (Fig. 10b) showing only the elements constituting for the HfN film (Hf and N peaks), indicating that it is a non-corrode zone, which indicates that in this zone the films acted as a diffusion barrier protecting the steel substrate against the corrosive ions (Cl^-). On the other hand, Fig. 10c and Fig. 10d show an EDX spectrum for zone 2 and zone 3, respectively. From this micrograph it was possible to observe the elements

constituting for the steel substrate (Fe, Mn, C and Cr peaks), Table 1, which indicates an exposition of steel substrate. Also in the EDX spectra it was found on the corroded surface (Fig. 10c) some traces of corrosive solution composed by Cl^- ions which is characteristic for this electrochemical system due to the adsorption process generated by the diffusion effect. In this way, taking in account the differences on gray scale from SEM results (Fig. 10a) was possible to estimate the ratio between corroded and non-corroded areas in order to get an idea of the film protective ability from microscopic data. Therefore, in this work it was estimated the corroded/non-corroded areas ratio was around 1.5.

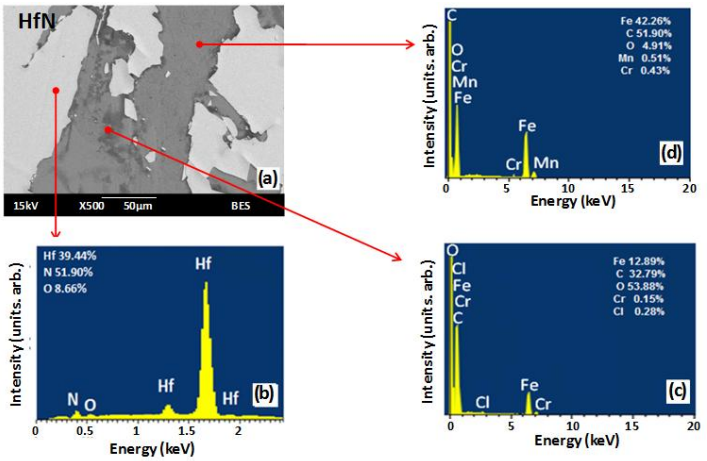

Figure 10. SEM micrograph and EDX spectra for the HfN/steel system after the corrosive Tafel test (a); zone 1(b), zone 2(c) and zone 3(d).

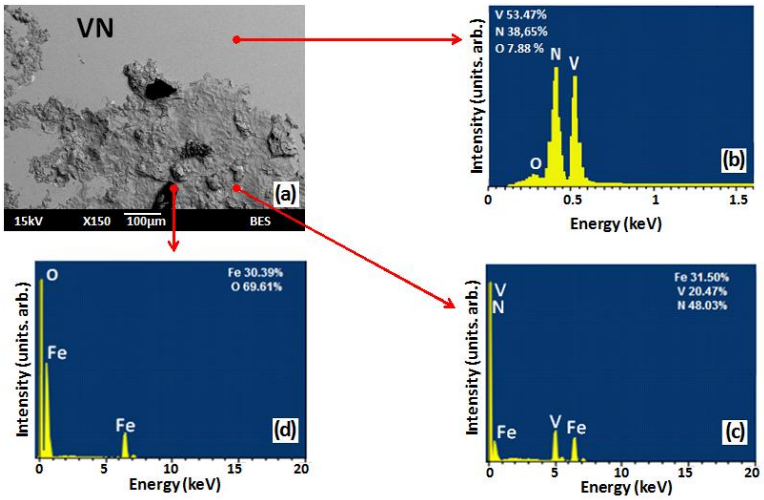

Figure 11. SEM micrograph and EDX spectra for the VN/steel system after the corrosive Tafel test(a); zone 1(b), zone 2(c) and zone 3(d).

Figure 11a shows a SEM micrograph for the VN/steel system after the corrosive Tafel test. From the micrograph results it was possible to identify three (3) zones in the same manner as was shown for the HfN/steel single layered system. EDX spectra extracted for the zone 1 (Fig. 11b) shows the elements presents into VN films (V and N), which indicate that in this zone 1 the protective films

acted as a diffusion barrier increasing the charge transfer resistance of the anodic dissolution and protect the steel substrate against the corrosive ions (Cl^-). On the other hand, EDX spectra for zone 2 and zone 3 (Fig.11c and Fig. 11d, respectively) show the principal elements constituting for the steel substrate (Fe peaks) and some iron oxidation processes (Fe and O peaks), which indicate a dissolution reaction between the electrolyte and the steel substrate.

Moreover, in the similar case of VN film it is possible to estimate the corroded/non-corroded areas ratio is around 0.81, in order to get an idea of the films protective ability from microscopic results.

On the other hand, with the aim to corroborate the observed by SEM results, a porosity factor associated to the different coating was calculated in agreement with W. Tato [26] and J. C. Caicedo [5]. The bombardment due to applying a negative bias during deposition produces a number of intrinsic defects, such as phase and grain boundaries, and dislocations. However, the permeable defects are more detrimental to the corrosion performance, as they provide direct paths to allow the corrosive electrolyte to access the steel substrate [27,28]. Fundamentally, the porosity evaluation by electrochemical methods is based upon current density ratio, but takes into account that the potentiodynamic measurements are an indirect measurement of the electrochemical behavior system and the current density is inversely proportional to the polarization resistance, so the porosity factor can be expressed as:

$$P = \frac{R_{p,u}}{R_{p,r-u}} - \frac{R_{p,u}}{R_{p,r}} \quad (6)$$

Where P is the total coating porosity, $R_{p,u}$ is the polarization resistance of the substrate uncoated, $R_{p,r-u}$ is the measured polarization resistance of film-substrate system and $R_{p,r}$ is the polarization resistance of the film. Due to the polarization resistance, a passive film is usually much larger than that substrate, $R_{p,r} >> R_{p,u}$. Then, the porosity corresponds simply to the ratio of the polarization resistances of uncoated and coated steel substrates.

$$P = \frac{R_{p,u}}{R_{p,r-u}} \quad (7)$$

When the porosity factor is close to zero (0%) this effect indicates that the films act as an inert barrier against the corrosive solution, on the other hand, if the porosity factor is close to unity (100%) it indicates that the film does not act as a barrier for the diffusion of Cl^- corrosive ions and this behavior is attributed to the defects of the films (e.g., pores, cracks, etc.). The polarization resistance values used in the equation (7) corresponds to the values presented in Table 5. The analysis of porosity factor values for both HfN and VN films (Table 6), suggest that the porosity factor is close to zero, therefore, these single layers improve the corrosion resistance in aggressive environments.

Table 6. Porosity factor values

	HfN	VN
Porosity factor (%)	1.62	9.42

The solution (Cl^- ions)-steel interaction occurs through the coating defects (e.g., pores, cracks, etc.), which are characteristic of coatings obtained by techniques PVD [29], as was discussed in the previous porosity factor analysis. It is worth noting that around the corroded zones (zone 2 and zone 3) for both HfN and VN films a local delamination in the films surface (Fig. 10a and Fig. 11a) occurs, which is a result of upward stress generated by the corrosion products formed on the film's steel interface by reacting between steel and the corrosive solution (Fig. 9). The last effect was in agreement with SEM and EDX analyses supported by results obtained from electrochemical results. Thus, it is observed that the porosity factor is lower for HfN than VN due to the physical, morphological, microstructural and electrochemical nature present in HfN single film. As was observed previously by TEM and AFM analysis a lower interplanar distance, grain size and roughness, allows greater protection to corrosive attack of the steel substrate.

3.8. The protective efficiency film

The protective efficiency of the HfN and VN single layers is determinate observing the surface nature and taking into account the electrochemical nature, therefore, the protective efficiency factor associated with the different films in agreement with J. C. Caicedo and coworkers [30]; in this sense, the protective efficiency factor corresponds to the ratio of the difference between corrosion intensity of the uncoated steel substrate and the corrosion intensity for the coated steel substrate and corrosion intensity of the uncoated steel substrate, which is shown in the following equation:

$$Pf\,(\%) = \left(\frac{Icorr_S - Icorr_f}{Icorr_S} \right) \times 100 \qquad (8)$$

Where *Pf* is the protective efficiency factor, $Icorr_s$ is the corrosion intensity of the uncoated steel substrate, and *Icorrf* is the corrosion intensity of the coated substrate. The protective efficiency factor values obtained are present, replacing the electrochemical values on Eq. (8) for all HfN and VN films. The protective efficiency factor determined for HfN films (99.90%) is higher than the VN single layer (99.73%) deposited with the same r.f. negative bias voltages, evidencing the best protective nature corresponding to HfN material, moreover, these results are in agreement with SEM micrographs (Fig. 10 and Fig. 11), and the porosity factor values presented in Table 6.

Aiming to compare the protective efficiency film in this research, it was calculated the protective efficiency film written in terms of polarization resistance (Pf_{Rp}(%)). These values are obtained replacing the polarization resistance values on Eq. (9) for all HfN and VN nitride films. The analysis of protective efficiency factor values (Pf_{Rp}) applied in both single layers suggests that protective efficiency factor written in terms of polarization resistance to HfN films (98.37%) is higher than the VN films (90.57%).

$$Pf_{Rp}\,(\%) = \left(\frac{R_{p,r-u} - R_{p,u}}{R_{p,r-u}} \right) \times 100 \qquad (9)$$

where Pf_{Rp}(%) is the protective efficiency film written in terms of polarization resistance, $R_{p,u}$ is the polarization resistance of the substrate uncoated, $R_{p,r\text{-}u}$ is the measured polarization resistance of film-substrate system .Therefore, taking into account the last analysis of the protective efficiency film

written in terms of polarization resistance present lower values than the protective efficiency written in terms of corrosion intensity. This difference can be caused by the effect of polarization resistance of the substrate within $R_{p,ru}$.

Finally, it was observed in this work the correlation between the porosity factor and the protective efficiency written in terms of corrosion intensity and also in terms of polarization resistance for HfN and VN films. In this sense, the nitride layer (HfN) with the lowest porosity factor showed the highest protective efficiency, due to differences in crystal orientation, chemical, morphological, electrochemical characteristics.

4. CONCLUSION

Hafnium and Vanadium nitrides films were deposited successfully by r.f. magnetron sputtering. The preferential orientation for FCC HfN (111) and (200) of VN films was observed via XRD analysis. From EDX results it was possible to identify the chemical composition in both films ($V_{0.43}N_{0.57}$ and $Hf_{0.44}N_{0.56}$) it was found that both were overstoichiometric. The morphology and changes in the grain size were determined for HfN and VN films, establishing a homogeneous surface for both nitride films.

The electrochemical behavior was studied, observing for both nitride films low corrosion rates (0.205 μmy for HfN and 40.87 μmy for VN) and polarization resistance of 49.34 ($k\Omega \bullet cm^2$) for HfN and 8.49 ($k\Omega \bullet cm^2$) for VN, which means an increase of around 6 and 61 times for HfN films in relation to VN and AISI 4140 steel substrates, respectively, with a performance under corrosion processes, such as was presented by Tafel curves. These enhancement effects in the HfN films could be attributed to the lowest interplanar distance, grain size and surface roughness corroborated by TEM and AFM analysis, and the porosity factor values, this last finding suggests that the porosity factor decreased with the increasing of protective efficiency film values. Finally, the passivation of HfN and VN thin films generates a protective layer creating a higher resistance to corrosive events than an uncoated industrial AISI 4140 steel substrate.

ACKNOWLEDGEMENTS
This research was supported by "El patrimonio Autónomo Fondo Nacional de Financiamiento para la Ciencia, la Tecnología y la Innovación Francisco José de Caldas" undercontract RC-No. 275-2011 with Center of Excellence for Novel Materials (CENM).

References

1. J.C. Caicedo, C. Amaya, L. Yate, W. Aperador, G. Zambrano, M.E. Gómez, J. Alvarado-Rivera, J. Muñoz-Saldaña, P. Prieto, *Applied Surface Science*, 256, (2010) 2876
2. C. Amaya, W. Aperador, J.C. Caicedo, F.J. Espinoza-Beltrán, J. Muñoz-Saldaña, G. Zambrano, P. Prieto. *Corrosion Science*, 51, (2009) 2994
3. L. Yate, J.C. Caicedo, A. Hurtado Macias, F.J. Espinoza-Beltrán, G. Zambrano, J. Muñoz-Saldaña, P. Prieto. *Surface and Coatings Technology*, 203, (2009) 1904

4. J.E. Sanchéz, O.M. Sanchéz, L. Ipaz, W. Aperador, J.C. Caicedo, C. Amaya, M.A. Hernández Landaverde, F. Espinoza Beltran, J. Muñoz-Saldaña, G. Zambrano, *Applied Surface Science*, 256, (2010) 2380
5. J. C. Caicedo, L. Yate, G. Cabrera, W. Aperador, G. Zambrano, and P. Prieto, *Journal of Materials Science*, 46, (2011) 1244
6. M. Grizalez, E. Martinez, J. Caicedo, J. Heiras, and P. Prieto, *Microelectronics Journal*, 39, (2008) 1308
7. K. Kutschej, B. Rashkova, J. Shen, D. Edwards, C. Mitterer, and G. Dehm, *Thin Solid Films*, 516 (2007) 369
8. U. Wiklund, B. Casas, and N. Stavlid, *Wear*, 261 (2006) 2
9. N. Fateh, G. A. Fontalvo, G. Gassner, and C. Mitterer, *Wear*, 262 (2007) 9
10. R. Hubler, *Surface and Coatings Technology*, 159 (2002) 680
11. Z. Zhou, *Surface and Coatings Technology*, 183 (2004) 275
12. J.-S. Jeng, C.-H. Liu, and J. S. Chen, *Journal of Alloys and Compounds*, 486 (2009) 649
13. M. Rendón-Belmonte, J. T. Pérez-Quiroz, J. Terán-Guillén, J. Porcayo-Calderón, A. Torres-Acosta, G. Orozco-Gamboa, *Int. J. Electrochem. Sci*., 7 (2012) 1079 - 1092
14. K.-L. Ou, "Integrity of copper–hafnium, hafnium nitride and multilayered amorphous-like hafnium nitride metallization under various thickness," *Microelectronic Engineering*, vol. 83, no. 2, pp. 312-318, Feb. 2006.
15. M. Staia, D. Bhat, E. Puchi-cabrera, and J. Bost, *Wear*, 261 (2006) 540
16. J. C. Caicedo, C. Amaya, L. Yate, O. Nos, M. E. Gomez, and P. Prieto, *Materials Science and Engineering: B*, 171 (2010) 56-61
17. G. Cabrera, J. C. Caicedo, C. Amaya, L. Yate, J. Muñoz Saldaña, and P. Prieto, *Materials Chemistry and Physics*, 125 (2011) 576
18. A.A.C. Recco, I.C. Oliveira, M. Massi, H.S. Maciel, A.P. Tschiptschin, *Surface and Coatings Technology*, 202 (2007) 1078
19. D. J. Siegel, L. G. Hector, and J. B. Adams, "First-principles study of metal – carbide / nitride adhesion :," *Acta Materialia*, vol. 50, pp. 619-631, 2002.
20. M. Stern and A. L. Geary, *Electrochemical Society*, 104 (1957) 56
21. V. K. William Grips, H. C. Barshilia, V. E. Selvi, and K. S. Rajam, *Thin Solid Films*, 514 (2006) 204
22. J. E. B. Randles and D. J. Schiffrin, "Surface Tension of Dilute Acid Solutions," *Electrochemistry*, 62 (1966) 2403
23. C. S. Ni, L. Y. Lu, C. L. Zeng, and Y. Niu, *Corrosion Science*, 53 (2011) 1018
24. "Standard Practice for Calculation of Corrosion Rates and Related Information from Electrochemical Measurements," in *Annual Book of ASTM Standards*, 89 (2010) 1
25. C. Liu, Q. Bi, A. Leyland, and A. Matthews, *Corrosion Science*, 45 (2003) 1257
26. [W. Tato and D. Landolt, J. Electrochem. Soc. 145 (1998) 4173
27. C. Liu, Q. Bi, a Leyland, and a Matthews, *Corrosion Science*, 45 (2003) 1243
28. H. A. Jehn, "Improvement of the corrosion resistance of PVD hard coating – substrate systems," *Surface and Coatings Technology*, vol. 45, pp. 212-217, 2000.
29. H. Altun and S. Sen, *Surface and Coatings Technology*, 197, (2005)193
30. J. C. Caicedo, G. Zambrano, W. Aperador, L. Escobar-Alarcon, and E. Camps, *Applied Surface Science*, 258 (2011) 312